Section 7

Global and regional climate models, sensitivity and impact experiments, response to external forcing

The impact of the Arctic Sea Ice retreat on the Extratropical cyclones and anticyclones: atmospheric model simulations

M.G. Akperov[1], V.A. Semenov [1,2], I.I. Mokhov[1,3] and A. Lupo[3]

[1] A.M. Obukhov Institute of Atmospheric Physics, RAS, Moscow, Russia
[2] GEOMAR Helmholtz Centre for Ocean Research Kiel, Kiel, Germany
[3] Department of Soil, Environmental, and Atmospheric Sciences, University of Missouri, Columbia, USA

The Arctic region has been warming more than twice as fast as the other parts of the world during the last decades. The rapid Arctic warming is accompanied by the dramatic change of the Arctic sea ice cover. Recently, it has been suggested that such climatic changes might have led to the increase of anomalous weather events in winter over Eurasia. An example is anomalously cold spells over Eurasia associated with atmospheric blocking events. However, a large uncertainty remains concerning robustness of the observed relations and associated mechanisms of impact (Semenov and Latif, 2015). The main goal of this research is to explore the connection between the declining Arctic sea ice (most strongly expressed in the Barents-Kara Seas region) in cold season and change of cyclonic and anti-cyclonic activity over Eurasia using simulations with an atmospheric general circulation model (AGCM).

The simulations were performed with the ECHAM5 AGCM (Roeckner et al., 2003) using identical sea surface temperature climatology but different sea ice concentrations (SIC) for the periods corresponding to the high (1966-1969), low (1990-1995) and very low (2005-2012) SIC regimes in the Arctic as well as for the mean climatological SIC for 1971-2000. The duration of each simulation was 50 years.

For the regimes with high and very low SIC, a statistically significant increase of the number of long-living anticyclones (with lifetime of more than 5 days) over Northern Eurasia was found. Long-living cyclones exhibited different changes in their number depending on their intensity (Fig. 1).

The analysis of the spatial patterns of cyclonic and anti-cyclonic activity over Eurasia was performed. We found an increase of the frequency of cyclones over the central region of the European part of Russia (EPR) and anticyclones over the northern region of the EPR for the regimes with a high sea ice concentration in the Arctic. For the regime with very low SIC the shift of the frequency of cyclones and anticyclones towards the central part of Russia was found.

This work was supported by the Russian Foundation for Basic Research (14-05-31078, 14-05-00518 and 15-35-21061) and Russian Federation President Grant (MK 2693.2014.5).

References

Roeckner, E., et al., 2003: The atmospheric general circulation model ECHAM5. Part I: Model description, Rep. 349, Max Planck Inst. for Meteorol., Hamburg, Germany.

Semenov V.A., Latif M.,2015: Nonlinear Atmospheric Circulation Response to Multi-year Arctic Sea Ice Concentration Changes in 1966-2012. ERL (submitted).

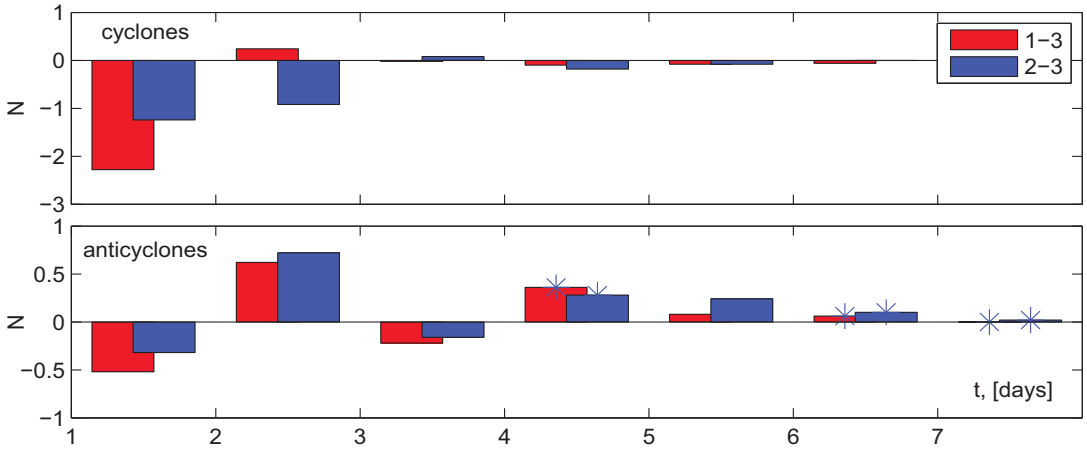

Fig. 1 Changes in the storm lifetime for 1966-1969 (1) and 2005-2012 (2) periods relative to the reference climate 1971-2000 (3).

The impact of convective parameterization schemes on the tropical precipitation diurnal cycle simulated by MRI-AGCM3

[1,2]Osamu Arakawa, [2]Hideaki Kawai and [2]Hiromasa Yoshimura
[1]University of Tsukuba, [2]Meteorological Research Institute, Japan Meteorological Agency
E-mail: oarakawa@mri-jma.go.jp

Nakamura (2009) showed that the precipitation diurnal cycle simulated by the Japan Meteorological Agency (JMA) short range forecast model over the Japanese islands in the boreal summer has its maximum in the evening, and this is in good agreement with the observations. Here, we compare the diurnal cycle of tropical precipitation simulated by the Meteorological Research Institute (MRI) global atmospheric model (MRI-AGCM3.2; Mizuta et al. 2012) with that in the observations from the viewpoint of the phase of the diurnal cycle; i.e., the timing of the daily precipitation maximum (and minimum). The model has three cumulus convective parameterization schemes: the Yoshimura scheme (Yoshimura et al. 2015, YMM); the prognostic Arakawa–Schubert scheme (Randall and Pan 1993, AS); and the Kain–Fritsch scheme (Kain and Fritsch 1990, KF). MRI-AGCM3.2 that uses the AS scheme is similar to the JMA short range forecast model. We conducted three experiments using MRI-AGCM3.2: (1) YMM (3.2YMM), (2) AS (3.2AS), and (3) KF (3.2KF). In these experiments the horizontal resolution of the model was a linear triangular truncation at wave number 319 (TL319), corresponding to the grid size of 60 km at the equator. The sea surface temperature (SST) and sea ice distribution given to the model were obtained from HadISST1.1. The period of numerical integration was 1979–2003. We compared the simulated 25-year average hourly precipitation with the observed 10-year climatology derived from the Tropical Rainfall Measuring Mission (TRMM) 3G68V7/PR gridded precipitation radar product, which only covered the period 1998–2007 because of restricted data availability.

Figure 1 shows the annual mean precipitation diurnal cycle for the tropics (30°S–30°N) over land and ocean. Over land, the observed precipitation has its maximum at 1600 local time (LT). However, the simulated precipitation in the 3.2YMM and 3.2KF runs has its maximum at 1400 LT, two hours earlier than that in the observations, that is a problem shared among global atmospheric models. In 3.2AS, precipitation has its maximum at 1700–1800 LT, 1–2 hours later than the observations. Minimum precipitation over land in all experiments is a few hours earlier than the observations (0900–1000 LT). Over ocean, observed precipitation reached its maximum (minimum) at 0500–0600 LT (1900–2000 LT). The diurnal cycle in all experiments of MRI-AGCM3.2 is close to that in the observations. In addition, oceanic precipitation in 3.2AS had a secondary maximum at 1400–1500 LT, and the observations showed a similar secondary maximum in the afternoon (1300 LT).

Over land, the precipitation maximum in run 3.2AS was a few hours later than in 3.2YMM and 3.2KF. The diurnal cycle in 3.2AS was similar to that in 3.2YMM and 3.2KF between midnight and 1000 LT. However, after 1000 LT the increase rate of hourly precipitation in 3.2AS was lower than that in 3.2YMM and 3.2KF. The reduced convective activity during the daytime in 3.2AS would be associated with the DCAPE scheme (Nakagawa 2008, Xie et al. 2000) introduced in 3.2AS.

To examine the impact of the DCAPE scheme on the precipitation diurnal cycle, we compared our results with the hourly precipitation simulated by MRI-AGCM3.1 (3.1AS; Kitoh et al. 2009), which uses AS as its convective parameterization but does not include the DCAPE scheme, under the same boundary conditions. Over land, the precipitation diurnal cycle in 3.1AS has its maximum (minimum) at 1400–1500 LT (0700 LT), which is similar to that in 3.2YMM and 3.2KF. Over ocean, on the other hand, the cycle in 3.1AS is similar to that in 3.2AS. The DCAPE scheme would delay the timing of precipitation diurnal cycle over land, although the fact that some of the physical processes used in MRI-AGCM3.1 differ to those in MRI-AGCM3.2 (e.g., the radiation scheme) may also change the timing of precipitation diurnal cycle. The mechanism that causes these differences remains unclear and should be the focus of future research.

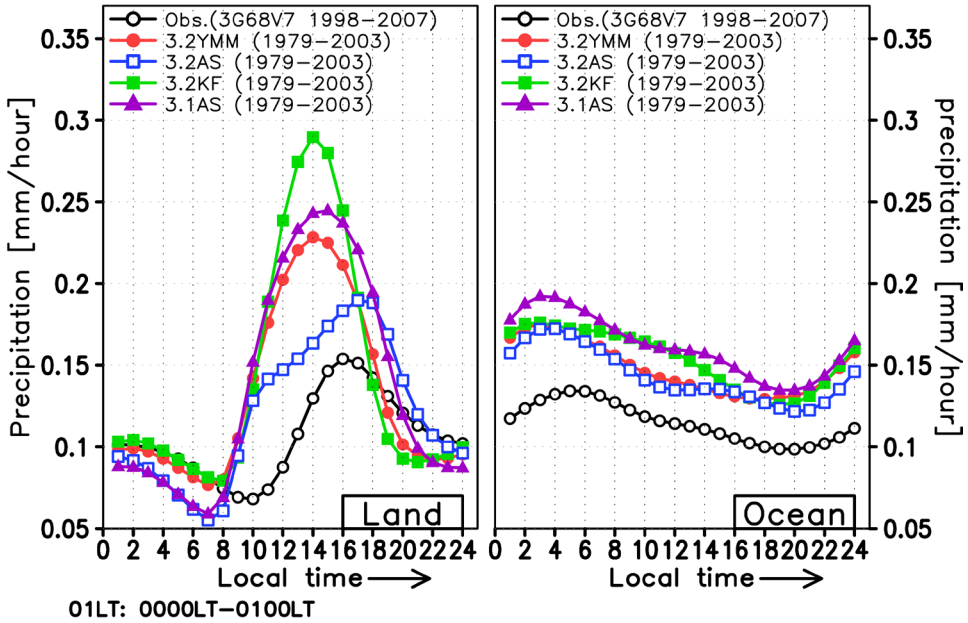

Figure 1: Annual mean precipitation diurnal cycle for the tropics (30°S–30°N) simulated by MRI-AGCM3 over land (left) and ocean (right). Units: mm/hour. Black line shows the observations (TRMM 3G68V7/PR). The red, blue, and green lines are MRI-AGCM3.2 with the Yoshimura (3.2YMM), Arakawa–Schubert (3.2AS), and Kain–Fritsch (3.2KF) schemes, respectively; the purple line is MRI-AGCM3.1 with the Arakawa–Schubert scheme (3.1AS).

Acknowledgements

This work was supported by the Program for Risk Information and Climate Change (SOUSEI program) funded by the Ministry of Education, Culture, Sports, Science and Technology (MEXT), Japan. We are grateful to Mr. E. Shindo, MRI, who introduced the KF scheme to MRI-AGCM3.2, and we would also like to express our gratitude to Dr. H. Murakami, GFDL/NOAA, for importing the DCAPE scheme into MRI-AGCM3.2.

References

Kain, J. S., and J. M. Fritsch, 1990: A one-dimensional entraining/detraining plume model and its application in convective parameterization. *J. Atmos. Sci.*, **47**, 2784–2802.

Kitoh, A., and co-authors, 2009: Projection of changes in future weather extremes using super-high-resolution global and regional atmospheric models in the KAKUSHIN Program: Results of preliminary experiments. *Hydrological Research Letters*, **3**, 49–53, doi:10.3178/hrl.3.49.

Mizuta, R., and co-authors, 2012: Climate simulations using MRI-AGCM3.2 with 20-km grid. *J. Meteor. Soc. Japan*, **90A**, 233–258.

Nakagawa, M., 2008: Improvement of the Cumulus Parameterization Scheme of the Operational Global NWP Model at JMA. *CAS/JSC WGNE Research Activities in Atmospheric and Oceanic Modelling*, **38**, 4.09–4.10.

Nakamura, T., 2009: Verification of quantitative precipitation forecasts over Japan from operational numerical weather prediction models. *CAS/JSC WGNE Research Activities in Atmosphere and Oceanic Modelling*, **39**, 6.13–6.14.

Randall, D., and D.-M. Pan, 1993: Implementation of the Arakawa Schubert cumulus parameterization with a prognostic closure. *Meteorological Monograph/The Representation of Cumulus Convection in Numerical Models*, **46**, 137–144.

Xie, S., C., and M. H. Zhang, 2000: Impact of the convective triggering function on single-column model simulations. *J. Geophys. Res.*, **105**, 14983–14996.

Yoshimura, H., R. Mizuta, and H. Murakami, 2015: A spectral cumulus parameterization scheme interpolating between two convective updrafts with Semi-Lagrangian calculation of transport by compensatory subsidence. *Mon. Wea. Rev.*, **143**, 597–621, doi:MWR-D-14-00068.1.

Simulation of the C-N cycles of the tundra ecosystem in the Northern Eurasia

M.M. Arzhanov
A.M. Obukhov Institute of Atmospheric Physics RAS
arzhanov@ifaran.ru

The carbon pool in the permafrost regions of the Northern Hemisphere is estimated at about 1.7 billion tons [1]. This pool exceeds more than twice the total amount of carbon in the atmosphere. At the end of the 20th century the rate of the annual mean temperature increase in the Arctic regions was 0.03°C per year [2]. According to simulations with global climate models [3-4], it may increase up to 0.05°C per year in the 21st century. As a result, an increase in the depth of the active layer is expected along with the inclusion of organic matter into the biogeochemical cycle in the thawed permafrost, which can lead to the emission of greenhouse gases into the atmosphere [5-6].

Soil carbon was measured at the experimental site of the tundra zone (67°22'N,78°37'E) for 07.2013-10.2013 [7]. To estimate carbon contents in the mineral soil, the Tyurin method for low organic carbon content was used. The measured vertical distribution of soil carbon (mean for six experimental sites) is shown in Fig. 1.

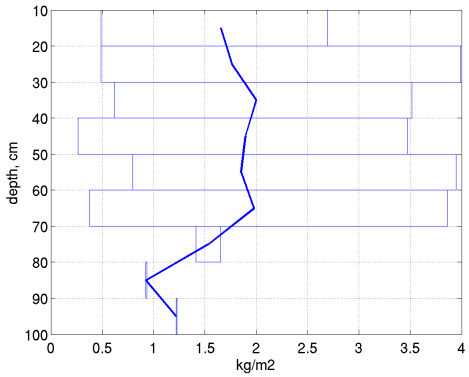

Fig. 1. The measured profile of soil carbon distributions in the mineral soil of the tundra zone (67°22'N,78°37'E). The blue bars show the observed range of soil carbon content at experimental sites.

According to the instrumental observations, the organic matter density in the upper one-meter soil layer in the ecosystems of Siberia, Alaska, Canada, and Tibet varies in a rather wide range from 2–8 to 9–14 kg C m^{-2} [8].

A one-dimensional version of the plant-soil model [9] was used. The distance between the vertical model levels in the soil was set to 10 cm in numerical simulations. The depth of the soil column in the experiments was 200 cm and the model time step was 1 day. The simulated soil carbon and nitrogen profiles in the equilibrium case are shown in Fig. 2.

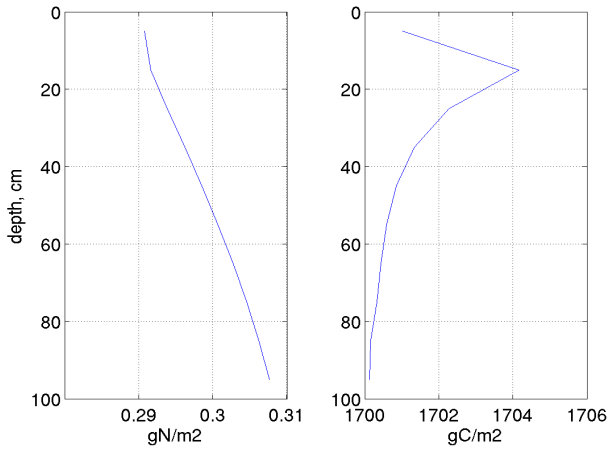

Fig. 2. The simulated profiles of soil carbon (left) and nitrogen (right) in the first meter of soil.

The carbon content in the first meter of soil estimated from model simulations was about 1.7 kg C m^{-2}. This agrees with observations (Fig. 1), 1.77±1.21 kg C m^{-2}.

Acknowledgements
The study was supported by the Russian Foundation for Basic Research (14-05-93089, 14-05-00201, 14-05-00518, 14-05-00193, 15-05-02457, 15-35-21061), the program of the Earth Sciences Department of the Russian Academy of Sciences.

References
1. Schuur, E. A. G., J. Bockheim, J. G. Canadell et al. (2008), Vulnerability of Permafrost Carbon to Climate Change: Implications for the Global Carbon Cycle, *Bioscience 58(8), 701–414*.
2. Pavlov, A. V. and G. V. Malkova (2009), Small-scale mapping of trends of the contemporary ground temperature changes in the russian north, *Kriosfera Zemli 13(4), 32–39*.
3. Arzhanov, M.M. and I.I. Mokhov (2013), Temperature Trends in the Permafrost of the Northern Hemisphere: Comparison of Model Calculations with Observations, *Doklady Akademii Nauk, 449(1), 87–92*.
4. Arzhanov, M.M., A.V. Eliseev, V.V. Klimenko, I.I. Mokhov, A.G. Tereshin (2012), Estimating Climate Changes in the Northern Hemisphere in the 21st Century under Alternative Scenarios of Anthropogenic Forcing, *Izvestiya AN. Fizika Atmosfery i Okeana, 48(6), 643–654.*
5. Arzhanov, M.M. and I.I. Mokhov (2014), Model Assessments of Organic Carbon Amounts Released from LongTerm Permafrost under Scenarios of Global Warming in the 21st Century, *Doklady Akademii Nauk, 455(3), 328–33.*
6. Arzhanov, M.M, P.F. Demchenko, A.V. Eliseev, I.I. Mokhov (2010), Modelling of subsidence of perennially frozen soil due to thaw for the Northern Hemisphere during the 21st century, *Kriosfera Zemli 14(3), 37-42.*
7. Kazantsev, V.S., E.A. Zarov, S.V . Loyko, M.M. Arzhanov, L.L. Golubyatnikov, S.N. Denisov N.N. Zavalishin (2013), Instrumental measurements of methane fluxes and stocks of soil organic in tundra ecosystems, *XVII Russian Conference "Composition of the atmosphere. Atmospheric electricity. Climate Processes". N. Novgorod. p. 36.*
8. Jobbagy, E.G. and R.B. Jackson (2000),The vertical distribution of soil organic carbon and its relation to climate and vegetation, *Ecological Applications, 10(2), 423– 436.*
9. Stieglitz, M., R.B. McKane, C.A. Klausmeier (2006), A simple model for analyzing climatic effects on terrestrial carbon and nitrogen dynamics: An arctic case study, *Glob. Biogeochem. Cycles, 20, GB3016, doi:10.1029/2005GB002603.*

Estimates of changes in the methane emissions from subpolar regions of Northern Eurasia in XXI century

S.N. Denisov, M.M. Arzhanov
A.M. Obukhov Institute of Atmospheric Physics RAS
denisov@ifaran.ru

The surface air temperature has been growing over land at high latitudes in the last few decades. This effect increases the permafrost temperature in some parts of the sub-Arctic region of Eurasia [1, 2]. In its turn, higher temperatures in the upper soil layers may lead to higher rates of decomposition of organic material and, consequently, to an increase in the greenhouse gases emission to the atmosphere from the soil [3]. A number of numerical experiments were conducted with a dynamical model of heat and moisture transfer in the soil forced by the RCP scenarios of anthropogenic impact. The areas where the soil temperature is to increase significantly (by more than 0.04 C/yr) in the 21st century were identified. The minimum trends (less than 0.01 C/yr) of soil temperature were obtained in the northern part of Eastern Siberia. According to the RCP 2.6 scenario, the thawed layer thickness increases by more than 1 m on the southern border of the permafrost in Western and Eastern Siberia as well as in the Tibet. The smallest increase in the thawed layer thickness is found for the north-western regions of central Siberia. For the most aggressive anthropogenic scenario RCP 8.5, the thawed layer thickness increases by more than 5 m in Western Siberia and the Baikal region. The increase in the thaw depth leads to the involvement of the organic matter conserved in permafrost to the global biogeochemical cycle.

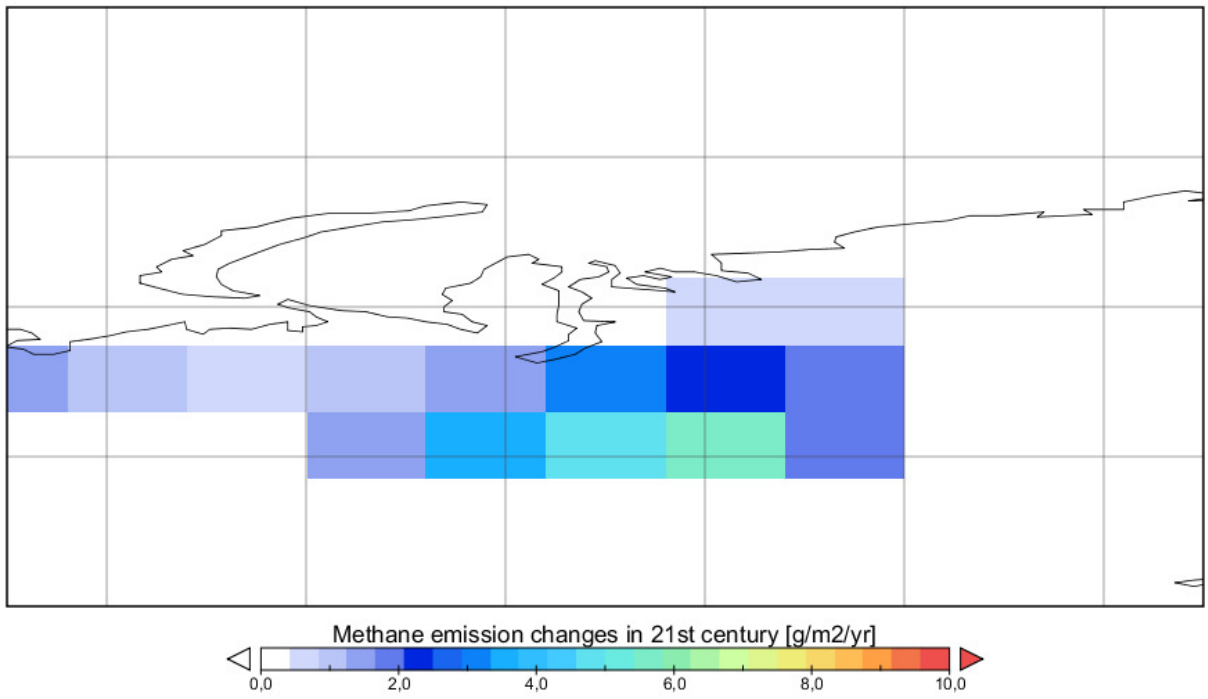

Fig.1 Changes in methane emission in the northern Siberia in the 21st century for the RCP 8.5 anthropogenic scenario.

A model of methane emission from wetlands, which takes into account the amount of soil carbon substrate in soil for the methane production [4-6], was used to estimate the changes in methane emissions from wetlands in Northern Eurasia in the 21st century under different scenarios of anthropogenic impact. For the most aggressive RCP 8.5 scenario of anthropogenic impact, the methane emissions more than tripled in this region; the largest increase in emissions (up to 10 mgCH4 / m2 / year) was obtained for the northern regions of Western Siberia (Fig. 1).

This work was supported by RAS programs and RFBR projects (15-05-02457, 14-05-00193, 15-35-21061, 14-05-93089, 14-05-00201).

References

1. Arzhanov M.M., Eliseev A.V., Mokhov I.I. A global climate model based, Bayesian climate projection for northern extra-tropical land areas // Glob. Planet. Change. 2012. V.86-87. P.57-65.
2. Eliseev A.V., Demchenko P.F., Arzhanov M.M., Mokhov I.I. Transient hysteresis of near-surface permafrost response to external forcing // Clim. Dyn. 2014. V.42. P.1203-1215.
3. Arzhanov M.M., Denisov S.N., Kazantsev V.S. Benchmarking Deep Soil Simulator against permafrost thermal characteristics measurements // Research Activities in Atmospheric and Oceanic Modelling. A. Zadra (ed.). WCRP. 2014. WCRP Report No.11/2014. P.7-03.
4. Denisov S.N., Kazantsev V.S., Arzhanov M.M. Changes in wetland methane emissions in the IAP RAS global model under RCP anthropogenic scenarios // Research Activities in Atmospheric and Oceanic Modelling. A. Zadra (ed.). Geneva: WCRP. 2013. WCRP Report No.10/2013. P.07.9-10.
5. Melton J.R., Wania R., Hodson E.L., Poulter B., Ringeval B., Spahni R., Bohn T., Avis C.A., Beerling D.J., Chen G.,Eliseev A.V., Denisov S.N., Hopcroft P.O., Lettenmaier D.P., Riley W.J., Singarayer J.S., Subin Z.M., Tian H., Zurcher S., Brovkin V., van Bodegom P.M., Kleinen T., Yu Z.C., Kaplan J.O. Present state of global wetland extent and wetland methane modelling: conclusions from a model intercomparison project (WETCHIMP) // Biogeosciences. 2013. V.10. N.2. P. 753-788.
6. Wania R., Melton J.R., Hodson E.L., Poulter B., Ringeval B., Spahni R., Bohn T., Avis C.A., Chen G., Eliseev A.V., Hopcroft P.O., Riley W.J., Subin Z.M., Tian H., Brovkin V., van Bodegom P.M., Kleinen T., Yu Z.C., Singarayer J.S., Zurcher S., Lettenmaier D.P., Beerling D.J., Denisov S.N., Prigent C., Papa F., Kaplan J.O. Present state of global wetland extent and wetland methane modelling: Methodology of a model intercomparison project (WETCHIMP) // Geosci. Model Devel. 2013. V.6. N.3. C.617-641.

Cloud feedbacks in MRI-CGCM3

Hideaki Kawai[1] (h-kawai@mri-jma.go.jp), Tsuyoshi Koshiro[1], Mark Webb[2], Seiji Yukimoto[1], and Taichu Tanaka[3]

[1]*Meteorological Research Institute, JMA*

[2]*UK Met Office Hadley Centre;* [3]*Japan Meteorological Agency*

1. Introduction

The cloud feedbacks in the MRI-CGCM3 (Yukimoto et al. 2012), which was used for CMIP5 simulations, were investigated. Changes in vertical profiles of cloud radiative effect (CRE), cloud cover, liquid and ice water content (LWC and IWC), and number concentrations of cloud droplets and ice crystals were examined. These profile changes were examined for several areas in which typical cloud regimes are dominant, to understand the contributions from each cloud regime to the global cloud feedback.

2. Model and Experiments

The model resolution is TL159L48 and the prognostic variables are cloud cover, LWC, IWC, and number concentrations of cloud droplets and ice crystals.

31 years averages (1979−2009) of data from AMIP and AMIP+4K runs are used for the analysis. AMIP and AMIP+4K run data of experiments with the convection scheme switched off, which was run under a project SPOOKIE (Webb et al. 2015b), are also examined to understand the roles of convection schemes for the cloud feedback in MRI-CGCM3.

The cloud feedback in MRI-CGCM3 for shortwave radiation is +0.43, for the longwave is −0.31, and the sum is +0.12 W/m^2/K. Figure 1 shows the CRE change for the sum of shortwave and longwave radiation at the top of the atmosphere.

3. Results

3.1. Global Mean

To understand the cloud feedback, the vertical profile of the CRE change was examined. The top left panel in Fig. 2 shows the CRE profile change for upward shortwave radiation. The CRE change is negative for 230 – 100 hPa, positive for 450 – 230hPa, negative for 900 – 700 hPa, and positive for surface – 900hPa, and the sum produces a positive shortwave cloud feedback in total. To understand the contribution of changes in cloud properties, vertical profiles of cloud cover, in-cloud LWC and IWC, in-cloud cloud droplet and ice crystal number concentrations were examined.

Above 230 hPa, the increases in cloud cover and in-cloud IWC contribute to the negative CRE change. The increase in cloud cover is mainly caused by higher top of deep convection, and the increase in in-cloud IWC is partly attributed to larger saturation specific humidity in AMIP+4K. For 450 – 230 hPa, decreases in cloud cover and in-cloud ice crystal number concentration, which overcome the increase in in-cloud IWC, contribute to the positive CRE change. It is plausible that the large increase in in-cloud LWC without significant change in cloud cover contributes to the negative CRE change at 900 – 700 hPa. The increase in in-cloud LWC is partly caused by the larger saturation specific humidity and the phase change of ice crystals to liquid droplets near 0 ºC

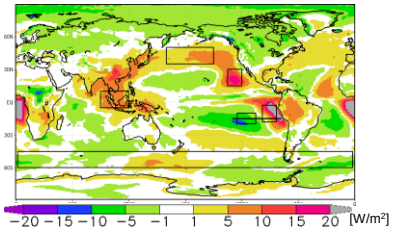

Fig. 1: CRE change for the sum of shortwave and longwave radiation at the top of the atmosphere (AMIP+4K – AMIP).

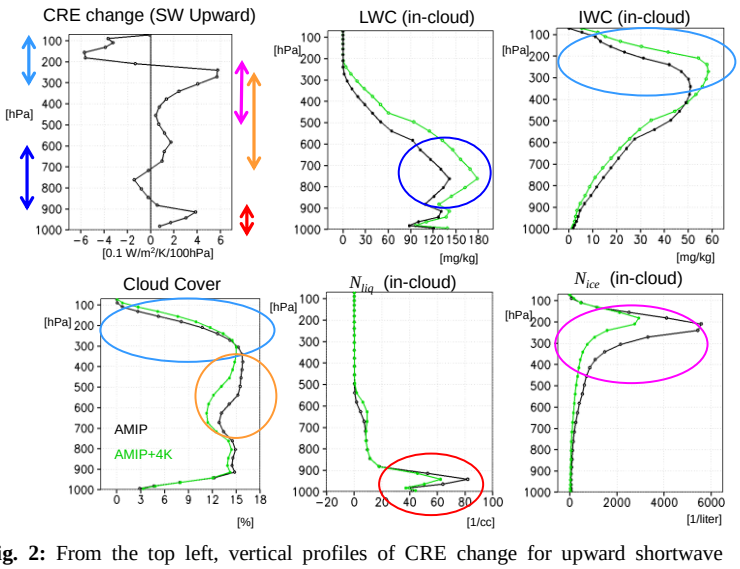

Fig. 2: From the top left, vertical profiles of CRE change for upward shortwave radiation from AMIP to AMIP+4K, in-cloud LWC and IWC, cloud cover, in-cloud cloud droplet and ice crystal number concentrations (black: AMIP, green: AMIP+4K). Global average for 31 years data.

altitude in AMIP+4K. Below 900 hPa, the positive CRE change is likely caused by reduction in the number concentration of cloud droplets. Some of these characteristics of changes related to clouds in MRI-CGCM3 are briefly mentioned in Webb et al. (2015a).

3.2. Changes in typical areas

To understand contributions from typical cloud regimes to the global average profiles, results from some areas are described below.

3.2.1. Deep convection area

Figure 3 shows that cloud cover is significantly reduced for 700 – 170 hPa in the AMIP+4K experiment in the Indochina area shown in Fig.1. This decrease is consistent with a reduction in relative humidity (figure not shown). The stronger drying by convective processes plausibly contributes to the change. Though the convection-off experiment shows similar characteristics to some extent, the change is much smaller than in the convection-on experiment.

3.2.2. Mid-latitudes

Figure 4 shows that cloud cover is reduced for 950 – 300 hPa in AMIP+4K experiment in the North Pacific area shown in Fig.1. The Convection-off experiment shows similar characteristics (except below 750hPa). Therefore, probably processes other than convection cause these changes. The results from the Southern Ocean area also shows similar characteristics (figure not shown).

3.2.3. Stratocumulus to Shallow Convection Area

Figure 5 shows that cloud cover associated with the shallow convection regime increases and stratocumulus cloud cover decreases in AMIP+4K. These changes are consistent with those in relative humidity, which are partly attributed to more intensive transport of humidity by shallow convection in AMIP+4K. When the convection scheme is switched off, the increase in cloud cover corresponding to shallow convection does not occur (figure not shown).

A large decrease in number concentration of cloud droplet is found in stratocumulus clouds, and this decrease contributes to the global average decrease shown in Fig.2. However, a bug related to number concentration equations could affect this large decrease, and so we will not discuss this change further. Note that the decrease in number concentration of cloud droplets is also found in a test run using a bug fix version, though the decrease is much less than in CMIP5 simulation.

3.3. Changes in aerosol concentrations

A large reduction in aerosol mass concentration is found in the AMIP+4K simulation at higher than 400hPa (figure not shown), which causes a reduction in calculated aerosol and ice nuclei number concentrations, contributing to a reduction in ice crystal number concentration. The reduction in aerosol can presumably be attributed to the increase in precipitation and decrease in convective mass flux over tropics in AMIP+4K simulation.

Acknowledgements

This work was partly supported by the Research Program on Climate Change Adaptation (RECCA) of the Ministry of Education, Culture, Sports, Science and Technology (MEXT), Japan, and the "Program for Risk Information on Climate Change".

References

Webb, M. J., et al., 2015a: The diurnal cycle of marine cloud feedback in climate models. *Clim. Dyn.*, **44**, 1419-1436.

Webb, M. J., et al., 2015b: The impact of parametrized convection on cloud feedback. in preparation.

Yukimoto, S., et al., 2012: A new global climate model of Meteorological Research Institute: MRI-CGCM3 -- model description and basic performance --. *J. Meteor. Soc. Japan*, **90A**, 23-64.

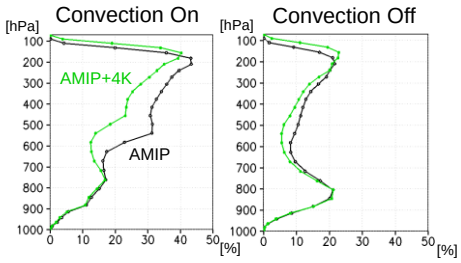

Fig. 3: Cloud cover profile for AMIP (black) and AMIP+4K (green) for the Indochina area shown in Fig. 1. Results of the normal model (left) and the convection switched off version are shown.

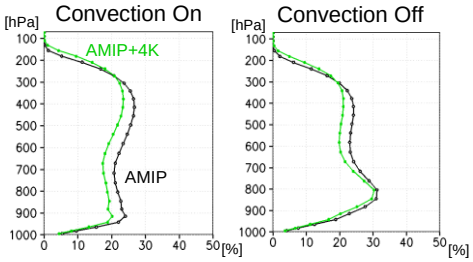

Fig. 4: Same as Fig. 3 but for the North Pacific area.

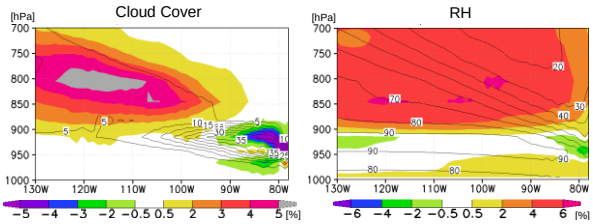

Fig. 5: Cross-sections of cloud cover (left) and relative humidity (right) along 15ºS shown in Fig.1 (shade: difference between AMIP+4K and AMIP, contour: AMIP climatology).

Hydrological anomalies and trends in the Amur River basin due to climate change

I.I. Mokhov, A.V. Chernokulsky, A.V.Timazhev, V.A. Semenov, V.C. Khon

A.M. Obukhov Institute of Atmospheric Physics RAS
mokhov@ifaran.ru

A record flood in the Amur River basin in 2013 was due to long intense rainfall in July-August. It was associated with the long atmospheric blocking anticyclone over the Pacific and with an extremely high surface temperature in the West Pacific. Key features of the Amur River basin are related to the East-Asian monsoon effects. An increase in the soil moisture during last years in the Far East regions facilitated an increase in the risk of anomalous floods in the Amur River basin [1-3].

Figure 1 shows meridional distributions of the summer blocking frequency in the Northern Hemisphere from reanalysis data for different years from 1969 to 2013 with dedicated distributions for 2013, 2010 and mean conditions [3]. The summer of 2013 (red curve) is characterized by high frequency of blocking activity over the Pacific.

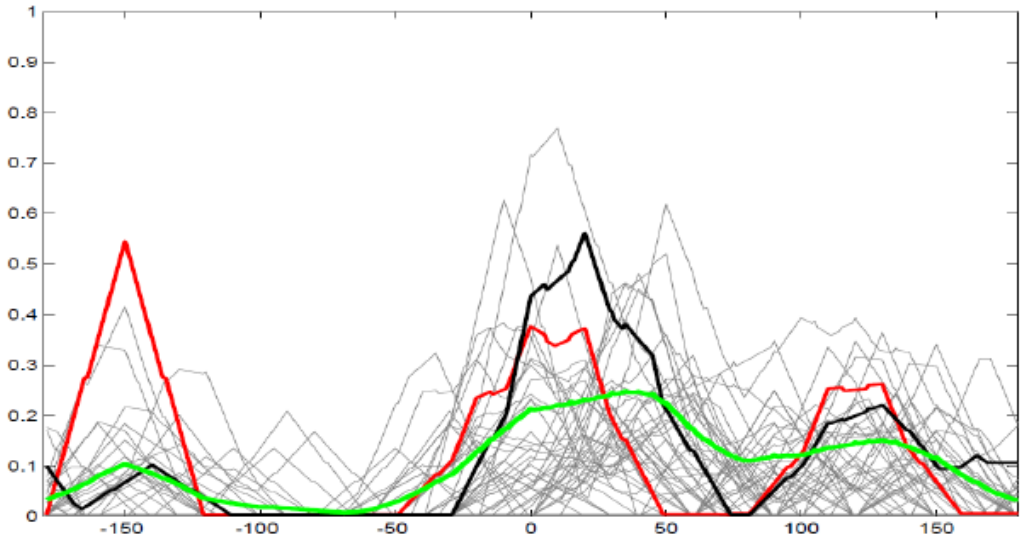

Figure 1. Meridional distributions of the summer blocking frequency in the Northern Hemisphere for different years during 1969-2013 with dedicated distributions for 2013 (red curve), 2010 (black curve) and mean conditions (green curve).

Long-lived atmospheric blockings over the Pacific during active periods of summer monsoon increase the risk of extreme phenomena in the Far East as it happened in 2013. With the general monsoons' intensification under global warming related to the increase in the atmospheric water-holding capacity and greater water vapor capacity of the atmospheric cyclones (with more intense rainfall), an increase in the risk of extreme floods in the Amur basin should be expected .

To assess possible changes, the CMIP5 multi-model simulations with RCP scenarios for the 21st century can be used. Figure 2 presents an example of estimates for trends in summer precipitation (mm/10 years) in the Northern Hemisphere from MPI-ESM-MR simulations with the RCP4.5 scenario for the 21st century (2006-2100) [3].

According to Fig. 2, the maxima of the summer precipitation trend in the 21st century are in the Far East, in particular in the Amur River basin. The obtained model estimates show an overall increase in the probability of extreme precipitation and runoff in the Amur River basin during monsoon seasons (summer - fall) under global

warming in the 21st century.

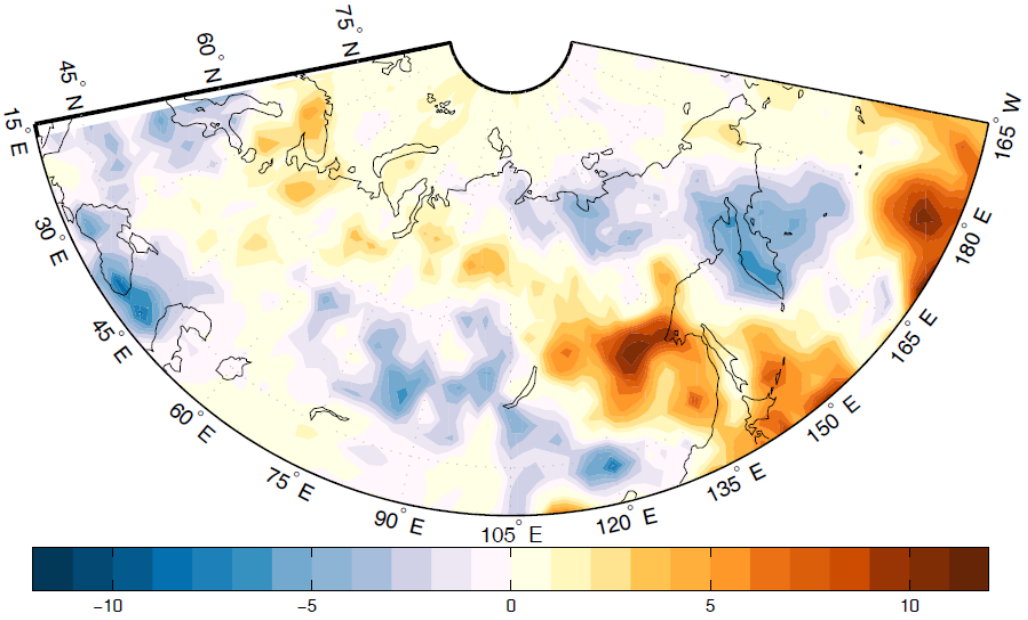

Figure 2. Estimated trends of summer precipitation (mm/10 years) in the 21st century (2006-2100) from climate model simulations (MPI-ESM-MR) with RCP4.5 scenario.

The risk of floods in the Amur River basin increases under global warming due to the possible increase of monsoon activity and total duration of summer blockings over the Pacific. A large uncertainty of the model estimates of possible hydrological changes in the Amur River basin should be also noted. It is related to the large natural variability of hydrological conditions (including runoff) in the Amur River basin observed since the end of the 19th century [3]. Significant effects associated with the Pacific Decadal Oscillation and El-Nino/Southern Oscillation are detected, in particular [3].

References

1. Mokhov I.I**.,** 2013: Hydrological anomalies and tendencies of change in the Amur River basin under global warming from model simulations. In: 8th Intern. Conf. on Atmospheric Physics, Climate and Environment, Sanya, China (17-20 November, 2013), 7.
2. Mokhov I.I., 2014: Hydrological anomalies and tendencies of change in the basin of the Amur River under global warming. *Doklady Earth Sci.*, 455 (2), 459-462.
3. Mokhov I.I., Khon V.C., Timazhev A.V., Chenokulsky A.V., Semenov V.A., 2014: Hydrological anomalies and tendencies of change in the Amur River basin in relation to climate changes. In: Extreme Floods in the Amur River Basin: Causes, Forecasts, and Recommendations. Moscow, Roshydromet, 81-120. (in Russian)

MESOPAUSE TEMPERATURE VARIATIONS: TENDENCIES OF CHANGE FROM OBSERVATIONS DURING LAST DECADES AND MODEL SIMULATIONS

Mokhov I.I.[1], Semenov A.I.[1], Volodin E.M.[2], Prokofyeva M.A.[1]

[1] A.M. Obukhov Institute of Atmospheric Physics RAS, Moscow
[2] Institute of Numerical Mathematics RAS, Moscow
mokhov@ifaran.ru

Temperature variations at the mesopause (MT) T_m measured in 1960-2014 at the Zvenigorod Scientific Station (56N, 37E) of the A.M. Obukhov Institute of Atmospheric Physics RAS (ZSS IAP RAS) are analyzed in comparison with variations of global surface air temperature (GSAT) δT_{gs} [1]. Long-term simulations with the INM-CM3.0 global climate model for the 20th-21st centuries are considered as well [2].

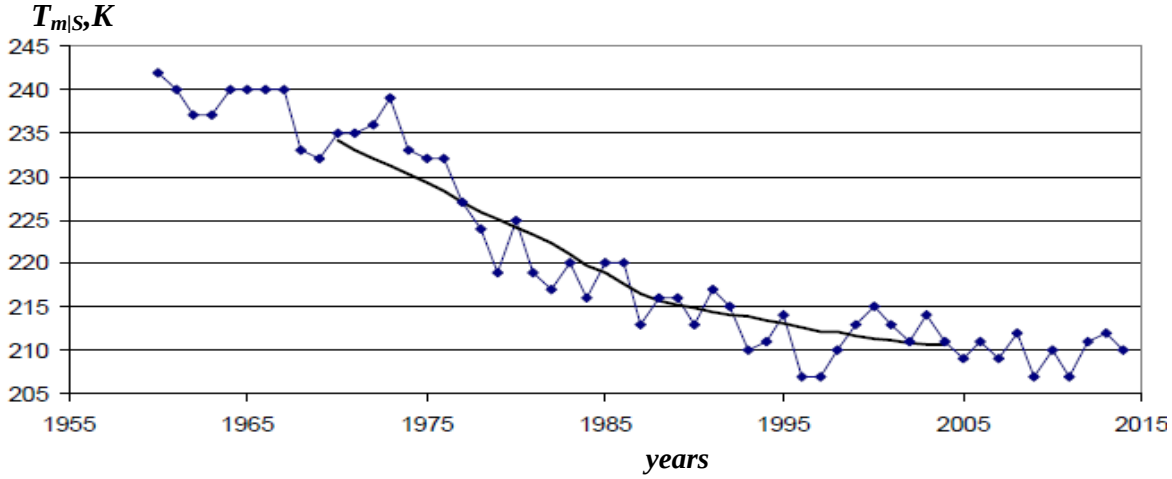

Fig. 1. The interannual $T_{m|S}$ variations (K) from winter observations at the ZSS IAP RAS during the period 1960-2014 (black curve - with 21-year moving averaging).

Figure 1 presents the interannual MT variations obtained from winter observations at the ZSS IAP RAS during the period 1960-2014; variations associated with solar activity S ($T_{m|S}$) are excluded. The interannual variations show a strong general decrease of Tm|S during the second half of the 20th century in winter (December-January-February) with a significant slowing of this cooling during the last decades.

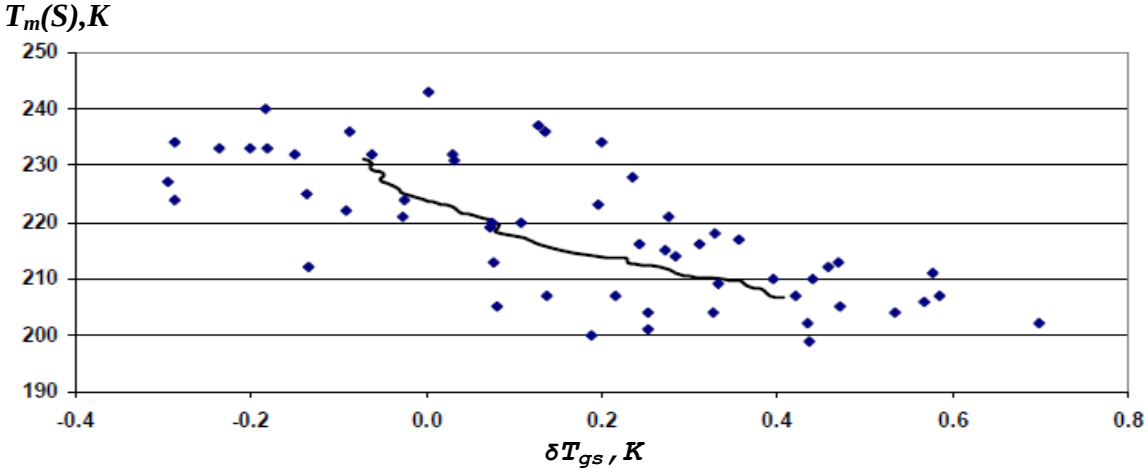

Fig. 2. The relationship between $T_m(S)$ variations from observations at the ZSS IAP RAS (K, ordinate) and variations of global surface temperature δT_{gs} (K, abscissa) in winter during the last 55 years (black curve - with 21-year moving averaging).

Figure 2 characterizes the relationship between MT variations obtained from the observations at the ZSS IAP RAS without excluding variations associated with solar $T_m(S)$ and GSAT variations (http://www.cru.uea.ac.uk/cru/data/temperature/) in winter during the last 55 years (1960-2014). A significant correlation between MT and GSAT was obtained for the whole time interval analyzed (1960-2014). There are essential differences for various decadal-scale intervals for the shorter intervals. It should be noted that the cross-wavelet analysis [3] did not reveal significant coherence of the most long-period variations in MT and GSAT for the analyzed data series. This is due to the relatively short length of the data series considered in the study.

To estimate the expected long-term coherence between MT and GSAT variations numerical simulations with global climate models can be used. Figure 3 shows the wavelet coherence between GSAT and MT (at the 0.005 hPa level) at 56N in winter found by INM-CM3.0 simulations with anthropogenic forcing according to the SRES-A2 scenario for the 21st century. Solid thin lines separate areas of edge effects, and solid thick lines bound the areas with local coherence at the 95% significance level.

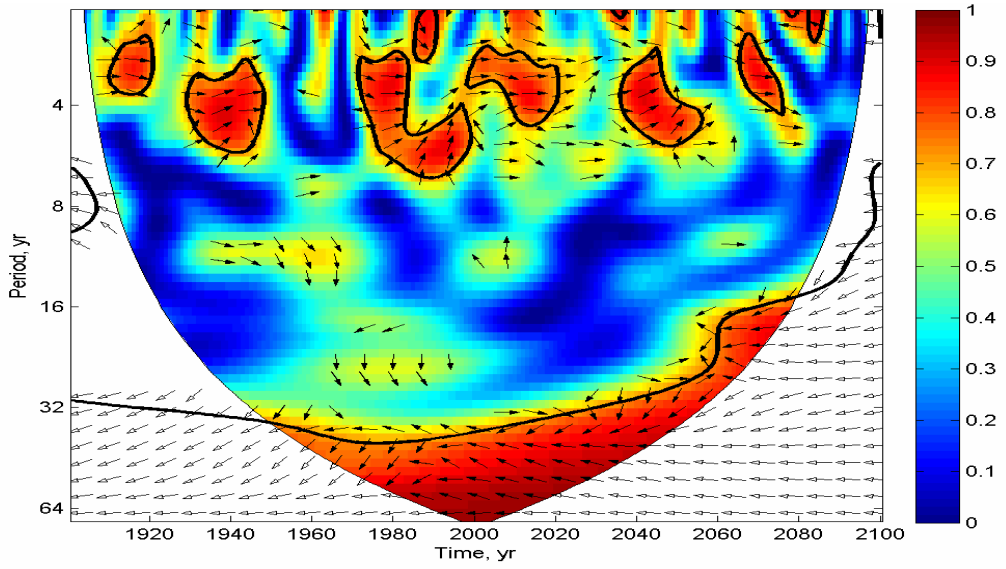

Fig. 3. Wavelet coherence between GSAT and MT (at the level 0.005 hPa) at the latitude 56N in winter from INM-CM3.0 simulations with anthropogenic scenario SRES-A2 for the 21st century.

The results of model simulations show the statistically significant negative coherence between MT and GSAT variations with periods larger than 3 decades. To display such a coherence from observations it is necessary to have at least twice longer data set for MT.

References

1. Mokhov I.I., Semenov A.I. (2014) Nonlinear temperature changes in the atmospheric mesopause region of the atmosphere against the background of global climate changes, 1960–2012. *Doklady Earth Sci.,* **456**(2), 741-744.
2. Galin V.Ya., Smyshlyaev S.P., Volodin E.M. (2007) Combined chemistry - climate model of the atmosphere. *Izvestiya, Atmos. Oceanic Phys.,* **43**(4), 437-452.
3. Jevrejeva S., Moore J.C., Grinsted A. (2003) Influence of the Arctic Oscillation and El Nino-Southern Oscillation (ENSO) on the conditions in the Baltic Sea: The wavelet approach. *J. Geophys. Res.,* **108**(D21), 4677, doi:10.1029/2003JD003417.

A phase shift between the changes of global temperature and carbon dioxide concentration in the atmosphere in a simple coupled climate-carbon cycle model

Muryshev K.E.[1], Timazhev A.V.[1,2]
[1]A.M. Obukhov Institute of Atmospheric Physics RAS
[2]Institute of Applied Physics RAS
kmuryshev@mail.ru

The atmosphere-ocean-land carbon dioxide exchange with periodic external forcings of different types is considered. The aim is to determine the phase shift between the global temperature and the atmospheric carbon dioxide concentration.

The coupled climate-carbon system is governed by the following equations:

$$C_0(dq/dt) = E(t) - F_{oc} - F_{land},$$

$$dD/dt = F_{oc},$$

$$d(M_b + M_s)/dt = F_{land},$$

$$C\,(dT/dt) = R_x \ln(q/q_0) + R(t) - \lambda T,$$

where q is the deviation of atmospheric CO_2 concentration from the preindustrial value q_0 = 278 pmm; D is the corresponding deviation of carbon stock in the ocean; M_b и M_s are the deviations of carbon stock in biota and soil, respectively; T is the temperature deviation; c_0 = 2.123 GtC/ppm; F_{oc} is the CO_2 flux from atmosphere to ocean; F_{land} is the CO_2 fluxes from atmosphere to land ecosystems; $C = 10^9$ J/m^2·K is the heat capacity per unit area; R_x = 5.34 W/m^2, λ = (0,82 ÷ 2,46) W/m^2·K is the feedback factor, $R(t)$ is the radiative forcing (RF), $E(t)$ is the external (e.g., anthropogenic) CO_2 emission to the atmosphere.

The CO_2 exchange between the atmosphere and the ocean is described by a Bacastow-type model but with temperature-dependent chemical constants in the ocean [Meier-Reimer E. and Hasselmann K., 1987]. The CO_2 flux from the atmosphere to land ecosystems and ocean is determined according to [Eliseev, Mokhov, 2007].

Numerical simulations were performed with the above-described model for different types of periodic forcing:

1) $R(t) = R_0 \sin(\omega t)$, $E(t) \equiv 0$;
2) $R(t) = R_0 \sin(\omega t)$, $E(t) = E_0 \exp(At)$.

Case 2) is modeling the situation in the 20th century.

In case 1) T can lag behind q or lead it depending on the forcing period. Long-period RF causes leading q, short-period RF causes leading T (Fig. 1).

In case 2) the result is identical to case 1). This result can be explained when considering the linearized model.

This work was supported by grant of Russian Federation government (the agreement 14.Z50.31.0033 with the IAP RAS) and by the Russian Foundation for Basic Research (projects 13-05-00652, 14-05-31163, 14-05-00639).

References:

1. Meier-Reimer E. and Hasselmann K. (1987). Transport and storage of CO2 in the ocean – an inorganic ocean-circulation carbon cycle model. *Climate Dynamics*, **2**, 63-90.
2. Eliseev A.V., Mokhov I.I. Carbon cycle-climate feedback sensitivity to parameter changes of a zero-dimensional terrestrial carbon cycle scheme in a climate model of intermediate complexity // Theor.Appl.Climatol. 2007. V.89. N.1-2. P.9-24.

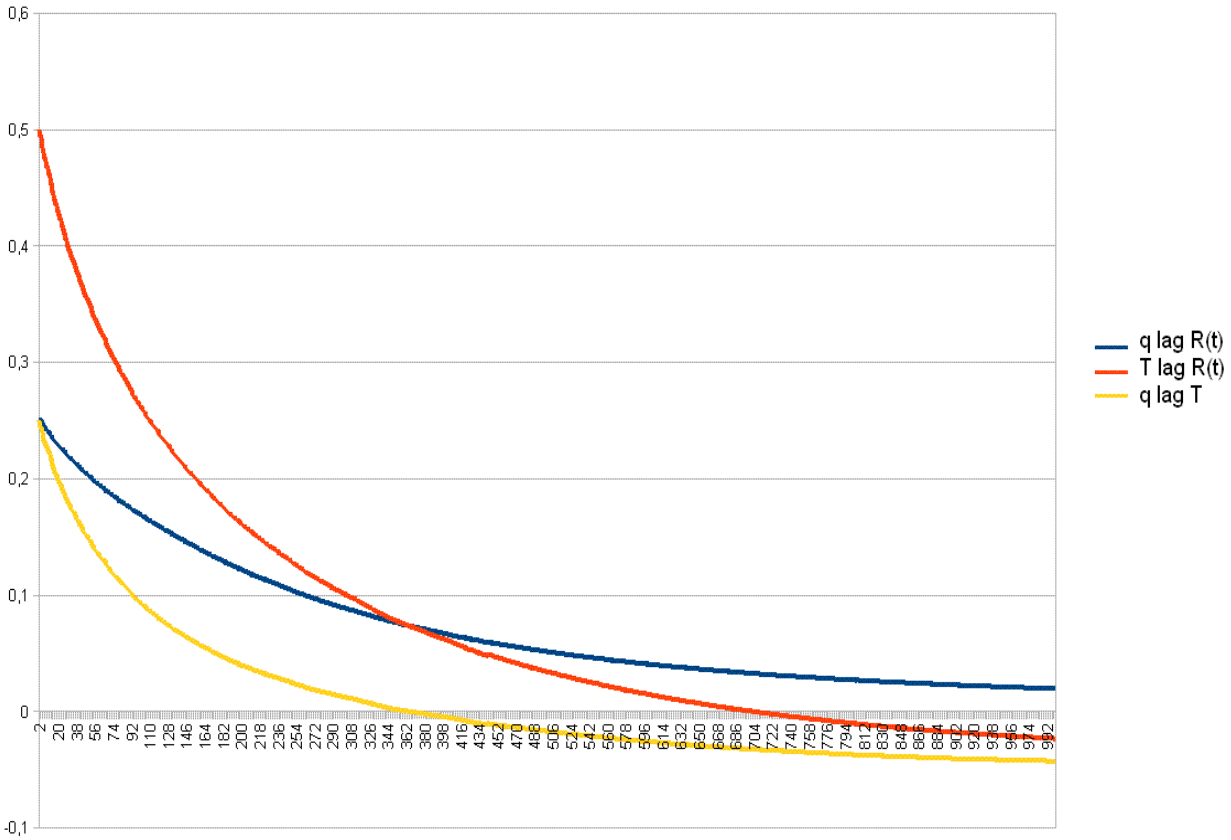

Figure 1. The phase shift divided to the RF period as a function of RF period (centuries).

Impact of Atlantic Multidecadal Oscillation on permafrost in the Northern Hemisphere estimated from idealized climate model simulations

Semenov V.A.[1,2], Arzhanov M.M.[1]

(1) A.M. Obukhov Institute of Atmospheric Physics RAS, 3, Pyzhevsky, Moscow, Russia
(2) Institute of Geography RAS, Moscow, Russia

vasemenov@mail.ru

Considerable reduction of the permafrost area and thawing depth in the Northern Hemisphere (NH) with global warming is projected in the 21st century by climate models (IPCC 2013). The permafrost changes have considerable effect on infrastructure and may also feedback to global climate through an increase of greenhouse gases emission from soil to the atmosphere from the decaying organic matter. While there are a number of studies estimating externally forced changes of permafrost in scenario climate models simulations, there is not much known about a possible range of permafrost changes caused by internal climate variations. The major part of internal long-term climate variability in the northern extratropics is related to the Atlantic Multiecadal Oscillation (AMO). AMO is linked to quasi-periodical oscillation of sea surface temperature (SST) in the North Atlantic and possible Arctic sea ice area with 60-70 year period (e.g., Schlesinger and Ramankutty 1995). AMO, in particular, has a significant impact on temperature and precipitation over Eurasia on decadal to multidecadal time scale (e.g., Mokhov et al. 2008).

Here, estimates of AMO impact on permafrost area and thawing depth in the NH based on climate model simulations are presented. We employ the atmospheric general circulation model ECHAM5 of T31 (3.8°x3.8°) spatial resolution coupled with mixed layer (50m) ocean model (Roeckner et al. 2003). Two 500 years long simulations are analyzed. One is a control, with climatological oceanic heat convergence fluxes (OHCF) and another is with additional AMO related OHCF. AMO is represented by periodically (60 yrs) varying anomalous OHCF in the NA and the Arctic. The AMO related flux pattern is the same is the one used in Semenov et al. (2010). Such an idealized simulation does not represent a full spectrum of internal ocean dynamics but allow one to disentangle the AMO effect. Main characteristics of permafrost are obtained using numerical scheme of heat and moisture transfer in the atmosphere-underlying surface-soil accounting for dynamics of frozen and thaw layers boundaries with water phase changes (Arzhanov et al. 2008). As an AMO index, SST anomalies average over 40N-60N,50W-10E box are used.

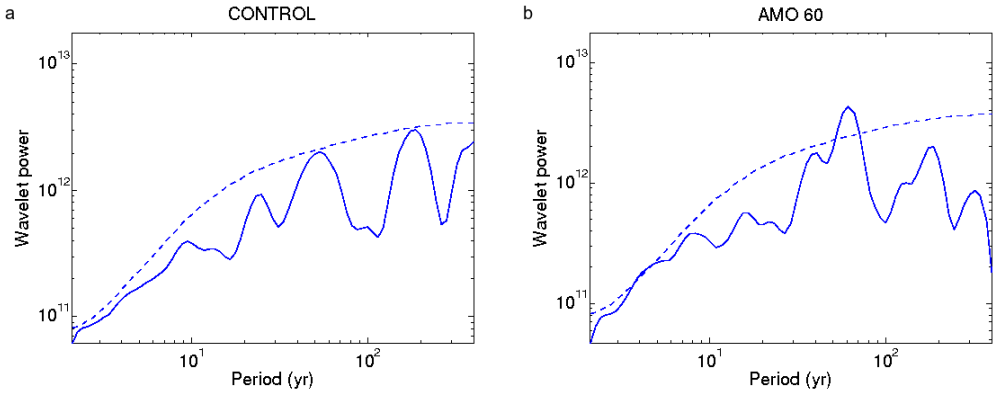

Fig.1. Wavelet spectra of NH permafrost area in control (a) and AMO-forced (b) simulations. Dashed lines show upper 95% confidence level of the fitted AR-1 process.

Variations of the NH permafrost area exhibit a statistically significant maximum at 60 yr period in the AMO-forced simulation that is absent in the control run (Fig.1). Amplitude of the NH area variations related to AMO transition from low to high phase amounts to 1.5 mln.km^2.

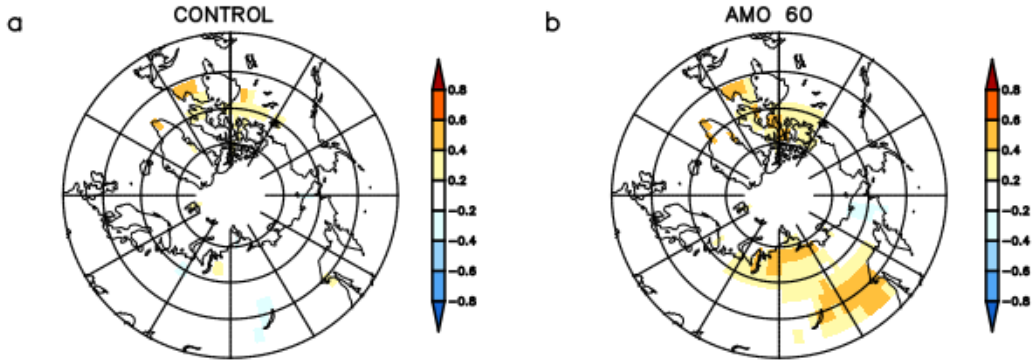

Fig.2. Correlation of the permafrost thawing depth with AMO index in control (a) and AMO-forced (b) simulations. All time series are smoothed with 11-yr running means.

AMO index in the AMO-forced simulations correlates with permafrost depth in the Eastern Eurasia and Canadian Archipelago with maximal correlations exceeding 0.4 (statistically significant at 90% confidence level) (Fig.2a). The control simulation does not reveal significant correlations over Eurasia despite comparable amplitude of internally caused AMO SST index variations (Fig.2a). Regression of the AMO index on thawing depth reaches 0.1m (not shown). Our analysis reveals a significant impact of AMO on the NH permafrost characteristics that is, however, considerably smaller than expected anthropogenically caused changes simulated by climate models to the end of the 21st century. The models project from 3 to 6 1.5 mln.km^2 area reduction depending on emission scenario (IPCC 2013)

This study was supported by Russian Science Foundation (14-17-00647).

References

Arzhanov M.M., Eliseev A.V., Demchenko P.F., Mokhov I.I., and Khon V.Ch. (2008) Simulation of thermal and hydrological regimes of Siberian river watersheds under permafrost conditions from reanalysis data. Izvestiya, Atmospheric and Oceanic Physics, 44, 83–89.

IPCC, 2013: Climate Change 2013: The Physical Science Basis. Contribution of Working Group I to the Fifth Assessment Report of the Intergovernmental Panel on Climate Change [Stocker, T.F., D. Qin, G.-K. Plattner, M. Tignor, S.K. Allen, J. Boschung, A. Nauels, Y. Xia, V. Bex and P.M. Midgley (eds.)]. Cambridge University Press, Cambridge, United Kingdom and New York, NY, USA, 1535 pp.

Mokhov I.I., Semenov V.A., Khon V.Ch., et al. (2008) Connection between Eurasian and North Atlantic climate anomalies and natural variations in the Atlantic Thermohaline Circulation based on long term model calculations. Dokl. Earth Sci., 419A (3), 502–505.

Roeckner, E., Bäuml, G., Bonaventura, L., et al. (2003) The atmospheric general circulation model ECHAM 5. Part I: Model description, Max Planck Inst. Meteorol., Hamburg.

Schlesinger M.E., Ramankutty N. (1995) An oscillation in the global climate system of period 65 – 70 years. Nature, 367, 723 – 726.

Semenov, V. A., Latif, M., Dommenget, D., et al. (2010) The impact of North Atlantic-Arctic multidecadal variability on Northern Hemisphere surface air temperature. Journal of Climate, 23, 5668-5677.